Research Square

Preprints are preliminary reports that have not undergone peer review.
They should not be considered conclusive, used to inform clinical practice,
or referenced by the media as validated information.

A multicentre longitudinal brain metastasis imaging dataset with lesion segmentations and clinical data

Yahir Y. Calderón-Silva

yahir.calderon@uclm.es

University of Castile-La Mancha https://orcid.org/0009-0008-5077-5054

Julián Pérez-Beteta

University of Castile-La Mancha https://orcid.org/0000-0003-0317-6215

David Molina-García

University of Castile-La Mancha https://orcid.org/0000-0002-6104-3894

Ismael Fernández-Hernández

University of Göttingen https://orcid.org/0000-0001-9833-919X

José D. Villanueva-García

University of Castile-La Mancha

Beatriz Ocaña-Tienda

University of Castile-La Mancha https://orcid.org/0000-0001-8931-3836

Silvia Bordel-Vozmediano

University of Castile-La Mancha https://orcid.org/0009-0008-5521-4993

Miguel Perales-Patón

University of Castile-La Mancha https://orcid.org/0009-0004-9749-6555

Beatriz Asenjo

Hospital Universitario de Málaga https://orcid.org/0000-0003-1299-5079

David Albillo

MD Anderson Cancer Center Madrid

Ana Ortíz de Mendivil

Hospital Universitario HM Sanchinarro https://orcid.org/0000-0002-3567-7041

Luis A. Pérez Romasanta

Hospital Universitario de Salamanca https://orcid.org/0000-0001-8117-5459

Elísabet González Del Portillo

Hospital Universitario Rey Juan Carlos https://orcid.org/0000-0002-0758-8156

Manuel Llorente

MD Anderson Cancer Center Madrid

Natalia Carballo

MD Anderson Cancer Center Madrid

Fatima Nagib-Raya

Hospital Universitario de Málaga https://orcid.org/0000-0003-3796-8093
María Vidal-Denis
Hospital Universitario de Málaga https://orcid.org/0000-0001-5316-3178
Belen Luque
University of Castile-La Mancha https://orcid.org/0009-0006-8931-6790
Zhao Hui Chen Zhou
Hospital Universitario 12 De Octubre https://orcid.org/0000-0003-0248-1066
Ana Ramos
Hospital Universitario 12 De Octubre
Rafael Morcillo
Hospital General Universitario de Ciudad Real https://orcid.org/0000-0003-4977-9302
Estanislao Arana
Fundación Instituto Valenciano de Oncología https://orcid.org/0000-0002-1884-7854
Víctor M. Pérez-García
University of Castile-La Mancha https://orcid.org/0000-0002-6575-495X

Research Article

Keywords: Brain Metastases, Brain Lesion, Segmentation, Magnetic Resonance Imaging, MRI, Surgery, Stereotactic Radiotherapy, Whole-Brain Radiotherapy, Systemic Treatment, Tumour, Radiomic

Posted Date: November 9th, 2026

DOI: https://doi.org/10.21203/rs.3.rs-11637027/v1

License: This work is licensed under a Creative Commons Attribution 4.0 International License.
Read Full License

Additional Declarations: The authors declare no competing interests.

A multicentre longitudinal brain metastasis imaging dataset with lesion segmentations and clinical data

Yahir Y. Calderón-Silva[1,2,3*], Julián Pérez-Beteta[1,2,3], David Molina-García[1,2,3], Ismael Fernández-Hernández[4], José D. Villanueva-García[1,2], Beatriz Ocaña-Tienda[1,2,3], Silvia Bordel-Vozmediano[1,2,3], Miguel Perales-Patón[1,2,3], Beatriz Asenjo[5], David Albillo[6], Ana Ortíz de Mendivil[8,9], Luis A. Pérez Romasanta[10], Elísabeth González Del Portillo[11], Manuel Llorente[7], Natalia Carballo[7], Fátima Nagib-Raya[5], María Vidal-Denis[5], Belen Luque[1,2], Zhao Hui Chen Zhou[12], Ana Ramos[12], Rafael Morcillo[13], Estanislao Arana[14,15†], Víctor M. Pérez-García[1,2,3†]

[1*]Mathematical Oncology Laboratory (MOLAB), Institute of Mathematics Applied to Science and Engineering, University of Castilla-La Mancha, Ciudad Real, 13071, Spain.
[2]Department of Mathematics, Escuela Técnica Superior de Ingeniería Industrial, University of Castilla-La Mancha, Ciudad Real, 13071, Spain.
[3]Mathematical Oncology Laboratory (MOLAB), Instituto de Investigación Sanitaria de Castilla-La Mancha (IDISCAM), Toledo, Spain.
[4]Department of Molecular Neurobiology of Behaviour, University of Göttingen, Göttingen, Germany.
[5]Radiology Department, Hospital Regional Universitario de Málaga, Málaga, Spain.
[6]Radiology Department, MD Anderson Cancer Center, Madrid, Spain.
[7]Radiation Oncology Department, MD Anderson Cancer Center, Madrid, Spain.
[8]CUHMED, Camilo José Cela University, Department of Neuroradiology, Hospital Universitario HM Sanchinarro, Madrid, Spain.
[9]CEU San Pablo University, Madrid, Spain.
[10]Radiation Oncology Department, Hospital Universitario de Salamanca, Salamanca, Spain.

[11]Radiation Oncology Department, Hospital Universitario Rey Juan Carlos, Móstoles, Spain.
[12]Radiology Department, Hospital 12 de Octubre, Madrid, Spain.
[13]Radiology Department, Hospital General Universitario de Ciudad Real, Ciudad Real, Spain.
[14]Radiology Department, Fundación Instituto Valenciano de Oncología, Valencia, Spain.
[15]School of Medicine, Catholic University of Valencia, Valencia, Spain.

*Corresponding author(s). E-mail(s): yahir.calderon@uclm.es;
Contributing authors: estanis.arana@ext.uv.es;
victor.perezgarcia@uclm.es;
†These authors were equally senior consultants.

Abstract

Brain metastases exhibit substantial variability in lesion burden, morphology and treatment response. Longitudinal imaging linked to lesion annotations and clinical histories can support quantitative studies of this heterogeneity. We describe a multicentre dataset from seven Spanish hospitals comprising 443 patients diagnosed between 2007 and 2022, with follow-up imaging for 216 patients. The collection contains 2842 magnetic resonance image, including 1092 three dimensional (3D) contrast-enhanced T1-weighted, 833 T2-weighted and 917 FLAIR (fluid-attenuated inversion recovery) images. Semiautomatic 3D-segmentation with expert review provides annotations for 1291 unique lesions represented by 2303 lesion observations across imaging time points. Separate labels identify contrast-enhancing and non-enhancing or necrotic tumour components, and lesion identifiers are maintained during follow-up. Accompanying records describe primary tumour characteristics, treatments, imaging dates and clinical outcomes, together with acquisition metadata and 107 morphological and radiomic features. The dataset supports research on lesion detection and segmentation, longitudinal response assessment, imaging biomarkers and mathematical models of brain metastasis growth and treatment response.

Background & Summary

Brain metastases (BMs) are the most frequent intracranial malignancies in adults and a major complication of systemic cancer, particularly lung cancer, breast cancer and melanoma[1, 2]. Their consequences extend beyond tumour burden: neurological deficits, seizures, cognitive impairment and treatment-related toxicity can substantially affect patients' daily functioning and quality of life. Intracranial disease may

comprise a solitary lesion or multiple metastases with different sizes, anatomical locations and treatment histories. This variability makes BMs an important setting for quantitative imaging research, where both the individual lesion and the patient's overall intracranial disease course need to be considered.

BMs develop through interactions between disseminated tumour cells and the brain microenvironment. Vascular structures, resident neural and glial cells, and immune populations influence metastatic colonisation and subsequent growth. The resulting biological properties and therapeutic responses cannot be inferred from the primary tumour alone[3]. Heterogeneity is also present within individual patients: lesions can emerge at different times and follow different trajectories during treatment. Capturing these changes requires repeated observations linked to persistent lesion identifiers. Longitudinal datasets therefore provide information that complements cross-sectional descriptions of tumour appearance and total intracranial burden.

Clinical management combines local and systemic approaches according to symptoms, lesion burden and location, primary tumour characteristics, extracranial disease and patient condition[4]. Surgery, stereotactic radiotherapy, whole-brain radiotherapy and systemic treatments address different aspects of disease control. Their effects must be assessed in the context of both intracranial progression and treatment-related morbidity. For example, the cognitive effects associated with whole-brain radiotherapy illustrate why radiological control is not the only relevant outcome[5]. For imaging research, these varied treatment pathways create a need to link lesion measurements to treatment timing, dose and fractionation, and the accompanying clinical history.

Magnetic resonance imaging (MRI) is central to BM detection, treatment planning and follow-up. Post-Contrast-enhanced T1-weighted (T1w+C) images show lesion boundaries and internal enhancement patterns, while T2-weighted (T2-W) and fluid-attenuated inversion recovery (FLAIR) images provide complementary information about surrounding tissue changes[6–8]. Interpretation becomes particularly challenging after treatment, when lesion enlargement or increased enhancement may reflect tumour progression, radiation-related injury, or overlapping processes. Radiation necrosis and recurrence can have similar appearances on conventional imaging. Serial changes in lesion volume and morphology provide an additional dimension for investigating these alternatives, as illustrated by previous studies of growth dynamics[9–11].

Reliable quantitative analysis depends on annotations that distinguish individual lesions and their constituent regions. Lesion segmentation enables localised analysis and provides global information about the lesion and its context within three-dimensional space. Meanwhile, radiomic features capture tissue and lesion properties, such as tumour volume, shape and texture, which can be translated into imaging and non-invasive biomarkers[12–14]. Creating such annotations requires substantial manual review, particularly for patients with numerous lesions or repeated examinations. Automated detection and segmentation methods seek to reduce this workload, but their development and evaluation depend on reference data with documented annotation procedures[15, 16]. Multicentre collections also expose algorithms to differences in acquisition protocols and scanners that may be obscured in more homogeneous datasets.

Longitudinal annotations are equally relevant to mathematical oncology. Measurements obtained before and after treatment can be used to estimate growth parameters, evaluate BM growth exponents and evolutionary dynamics, and assess whether proposed models accurately reproduce observed lesion trajectories[17, 18]. Combining mechanistic models with image analysis and statistical learning requires data that preserve the correspondence between patient, lesion, examination and treatment. Such resources can support the development of patient-specific models, including components of digital twins, while providing a basis for evaluating their assumptions and predictive limitations.

Public resources with segmented BMs now cover several complementary research settings. Stanford BrainMetShare provides multisequence MRI with radiologist-generated lesion masks for detection and segmentation research[15, 19]. The San Francisco Brain Metastases Stereotactic Surgery dataset (UCSF-BMSR) includes 560 MRI examinations from 412 patients undergoing stereotactic radiosurgery, with expert voxelwise annotations of 5136 metastases[20]. Pretreat-MetsToBrain-Masks provides pretreatment MRI with separate annotations of enhancing tumour, necrotic tissue and peritumoral FLAIR hyperintensity[21]. The multicentre BraTS-METS 2023 challenge established a benchmark for segmentation on pretreatment multiparametric MRI[22]; the 2025 challenge extended this scope to pre- and post-treatment imaging[23]. These resources differ in their annotation targets and treatment settings, which must be considered when comparing segmentation methods.

Other collections connect segmentation masks to more specialised clinical or biological information. The Cancer Imaging Archive hosts several such resources[24], including Brain-Mets-Lung-MRI-Path-Segs, which pairs MRI and regional annotations with histopathological images of lung-cancer BMs[25], and Brain-TR-GammaKnife, which includes treatment-planning and follow-up information[26]. The Metastatic Breast Cancer (BCBM-RadioGenomics) MRI dataset comprises 268 T1w+C MRIs of 165 patients. This collection includes segmented mask for tumour, of postoperative tumour bed/reserction cavity, and neighbouring at-risk structures, as well as radiomic features[27]. A multi-center, multi-origin brain tumor MRI (MOTUM) contains both primary brain tumours and BMs, with enhancing-tumour and non-enhancing FLAIR-abnormality masks, pathological information and radiomic measurements[28]. More recently, the Brain mEtAsetases segmentation for STEreotactic Radiotherapy (BEAMSTER) dataset released T1w+C MRI from 140 patients treated with stereotactic radiotherapy, with radiation-oncologist annotations of 260 metastatic lesions[29].

Longitudinal resources address the additional challenge of relating imaging changes to disease course and treatment. NYUMets-Brain combines serial MRI, expert segmentation annotations and clinical follow-up for longitudinal assessment[17]. Our previous dataset provided serial MRI, lesion segmentations, clinical information and radiomic measurements[30], while PROTEAS project links longitudinal MRI and tumour masks to clinical, radiomic and radiotherapy data[31]. However, the availability of repeated imaging does not, by itself, imply that every examination is annotated or that individual lesions have persistent identifiers. Therefore, the analyses that each collection can

support are determined by cohort selection, annotation coverage, tissue-label definitions, and links between lesions, examinations, and treatments. These considerations motivate the explicit documentation of lesion identity and follow-up in this research.

Collectively, this continuous trajectory of public resources has progressively expanded the scope of automated image analysis in cancer research. Building upon this base, the Open Brain Tumour dataset for Artificial Intelligence applications (OBTAI) provides a complementary infrastructure designed to integrate previously separated data dimension. This project unifies multicentre scanner variability, different primary tumour types, longitudinal continuity with unique lesion tracking, multiparametric MRI coverage, and comprehensive radiomic and morphological profiling within a single framework. Through this integration, OBTAI aims not only to support automated image analysis, but also to clear the way for refined clinical diagnosis, prognostic stratification, and non-invasive biomarker development.

Here, we describe OBTAI, a dataset developed within the METMATH study through collaboration with seven different clinical institutions. It comprises imaging and clinical information from 443 patients, including longitudinal imaging data for 216 patients and annotations for 1291 unique lesions, with 2303 observations across imaging time points. The set combines: three dimensional T1w+C, in what follows we denote it by (3D-T1w+C), T2-W and FLAIR images with manually reviewed 3D-segmentations, acquisition metadata, clinical records, morphological and radiomic features. It is intended to support lesion detection and segmentation, longitudinal response assessment, imaging biomarker research and mathematical modelling. This Data Descriptor documents the collection and processing methods, record structure, technical checks and considerations for reuse.

Methods

Study population and data collection

Data were collected restrospectively from seven collaborating hospitals. Patients were diagnosed with BMs between 2007 and 2022, and imaging and clinical information were collected during 2021–2024. Inclusion required deceased adult patients with a clinical or pathological diagnosis of BM and an available 3D-T1w+C MRI examination. Experienced radiologists assessed image quality; studies with substantial motion-related blurring or ghosting artefacts were excluded.

The cohort includes different primary tumour types and treatment management. Clinical variables include age at the first MRI examination, sex, primary tumour characteristics, lesion location and diagnosis date, treatment details, radionecrosis, surgery, and date and cause of death. The imaging collection includes pretreatment and follow-up examinations. A patient identifier links the clinical and imaging records, while a separate lesion identifier permits individual metastases to be followed over time. The collection is summarised in Table 1.

Data component	Number
Patient cohort	443
Patients with follow-up imaging	216
MRI sequence volumes	2842
3D-T1w+C	1092
T2-W	833
FLAIR	917
Unique annotated lesions	1291
Annotated lesion observations across imaging time points	2303
Morphological and radiomic features per analysed lesion observation	107

Table 1: Overview of the dataset. A sequence volume is a three-dimensional image acquired with three-dimensional spatial resolution. A lesion observation is the annotation of a unique lesion at a specific time during an imaging procedure. Several sequence volumes or lesion observations may belong to the same examination.

Ethical approval

We have complied with all relevant ethical regulations and all subjects included in the study are deceased. Human data were obtained in the framework of the OpenBTAI study (Open database of Brain Tumors for studies in Artificial Intelligence), a retrospective, multicentre, non-randomized study approved by the corresponding institutional review boards applicable to this dataset: Fundación Instituto Valenciano de Oncología (2021-05), Hospital Universitario HM Sanchinarro (21.06.1858-GHM), Hospital Universitario 12 de Octubre (21/711), Hospital General Universitario de Ciudad Real (12/2021), Hospital Regional Universitario de Málaga (24/06/2021), MD Anderson Cancer Center (01/06/2021), and Hospital Universitario de Salamanca (2021 10 879).

Image acquisition

MRI scans were acquired in routine clinical practice using scanners from General Electric (43.63%), Philips (28.57%), Siemens (25.62%), and no available information (2.18%), with reported field strengths of 1.0 (1.79%), 1.5 (88.38%), 3.0 T (7.52%), and no available information (2.31%). The 3D-T1w+C images were obtained after intravenous administration of a gadolinium-based contrast agent. T2-W and FLAIR images were also included where available. Acquisition protocols varied across centres and examinations.

Sequence-level acquisition metadata were extracted from Digital Imaging and Communications in Medicine (DICOM) headers. These include field strength, echo time, repetition time, slice thickness and spacing between slices. The metadata are provided in a separate comma-separated values (CSV) file to support assessment of acquisition heterogeneity. These parameters are summarised in Table 2

Sequence	Magnetic Field Strength (T)	Echo Time (ms)	Repetition Time (ms)	Slice Thickness (mm)	Spacing Between Slices (mm)
3D-T1w+C	1.0	6.9 (6.9–6.9)	25.0 (25.0–25.0)	1.6 (1.6–2.0)	0.8 (0.8–1.0)
	1.5	5.9 (1.5–16.9)	148.1 (5.9–2200.0)	1.4 (0.5–4.0)	0.9 (0.5–2.2)
	3.0	2.9 (2.4–5.2)	89.6 (5.7–2000.0)	1.1 (0.8–1.8)	0.9 (0.5–1.4)
T2-W	1.0	120.0 (120.0–120.0)	7030.1 (4742.3–7587.5)	4.1 (4.0–5.0)	4.8 (4.4–6.9)
	1.5	100.3 (9.9–135.5)	5732.4 (540.0–22580.5)	4.9 (1.0–6.0)	5.9 (0.5–8.0)
	3.0	83.1 (15.0–121.0)	3256.8 (500.0–5773.3)	3.9 (3.0–5.5)	4.5 (3.0–7.0)
FLAIR	1.0	140.0 (140.0–140.0)	11000.0 (11000.0–11000.0)	4.2 (4.0–5.0)	4.6 (4.4–5.4)
	1.5	128.4 (80.2–400.3)	9451.4 (4800.0–13200.0)	4.7 (1.0–6.0)	5.5 (0.5–8.4)
	3.0	154.8 (20.0–384.0)	9903.1 (2000.0–11002.0)	3.9 (1.0–6.0)	4.5 (0.7–7.5)

Table 2: Summary of parameters for the MRI sequences 3D-T1w+C, T2-W, and FLAIR. Results are presented as the median ($min - max$).

Clinical data collection and de-identification

Clinical information was obtained from the collaborating institutions and organised by patient and lesion. The variables and coding are described in Data Records. De-identification began at the contributing institutions and was followed by removal of identifying image metadata and assignment of study-specific patient identifiers using the OBTAI prefix. Lesion identifiers were maintained across follow-up examinations. No changes were made to the clinical and imaging dates in the released files, thus within-patient time intervals were preserved.

Image defacing

A two-phase defacing process was applied to remove the facial features from the imaging data. In the first stage, a You Only Look Once (YOLO) Deep Learning algorithm version 2 was used for real-time object recognition, utilizing raw images extracted directly from DICOM files (Figure 1). The image was partitioned into a grid of cells, each of which was responsible for detecting objects within its boundaries. YOLO then predicted a set number of fixed bounding boxes for each cell, with a confidence score representing the probability of the cell containing an object. For each of these boxes, YOLO predicted the probability of each object class using predictions

from a Convolutional Neural Network (CNN) trained on a labelled image dataset. Each slice of the selected images from the axial section was manually labelled and annotated using the graphical image annotation tool `Labeling` version 1.8.3. The sensitivity of the CNN to the quantity of images was tested using 4104 T1-weighted images in an axial orientation. These were divided in three groups: a training set of 400 images, a validation set of 100 images, and a test set of 3604 images.

A second stage was applied to the contrast-enhanced 3D-T1w+C images using a combination of Pydeface version 2.0.2 and the Brain Extraction Tool (BET) in FSL version 6.0.7.18. This methodology was applied to the main image in Neuroimaging Informatics Technology Initiative (NIfTI) format, independently of its orientation. An advanced skull-stripping process was performed on the input image to produce a brain-extracted image. This involved running `bet2` and `betsurf` to obtain additional skull and scalp surfaces. The output image provided a brain mask after the fractional intensity threshold was adjusted to range from 0.015 to 0.7, with the threshold gradient set to 0 in order to preserve anatomical and structural features of interest. A subsequent PyDeface algorithm was then performed using `template` and `facemask` to specify the registration target and the face mask image, respectively (Figure 2). This additional step addressed the limitations of the initial procedure with regard to residual facial features and orientation. The results were manually checked for each case and date.

Image conversion and spatial consistency

DICOM images were converted to NIfTI format using `dicom2nifti` version 2.4.10 and `dcm2niix` version 1.0.20241211 with Python version 3.12.2. Image and segmentation geometry was handled using NiBabel version 5.3.2 and FSL version 6.0.7.18. The NIfTI affine maps voxel indices to physical coordinates and includes voxel scaling, orientation and translation[32]. In homogeneous coordinates, this mapping is

$$\begin{bmatrix} x \\ y \\ z \\ 1 \end{bmatrix} = A \begin{bmatrix} i \\ j \\ k \\ 1 \end{bmatrix}, \tag{1}$$

where (i, j, k) are voxel indices, (x, y, z) are physical coordinates and A is the image affine matrix.

Images and their associated masks were reoriented to the closest canonical orientation. The image affine matrix was extracted using `nifti.affine` and used to generate the corresponding mask affine matrix, with updates to the voxel arrays and affine information. This process ensures spatial consistency between image base and the mask file, which therefore share the same spatial geometry. Also the right–anterior–superior convention was applied to all registration, thereby establishing a common anatomical template. The `qform` and `sform` transformations and their associated codes were considered when checking spatial consistency with `numpy.linalg.norm` version 2.5, ensuring the differences between these vectors were less than a tolerance of $(5 \cdot 10^{-2})$.

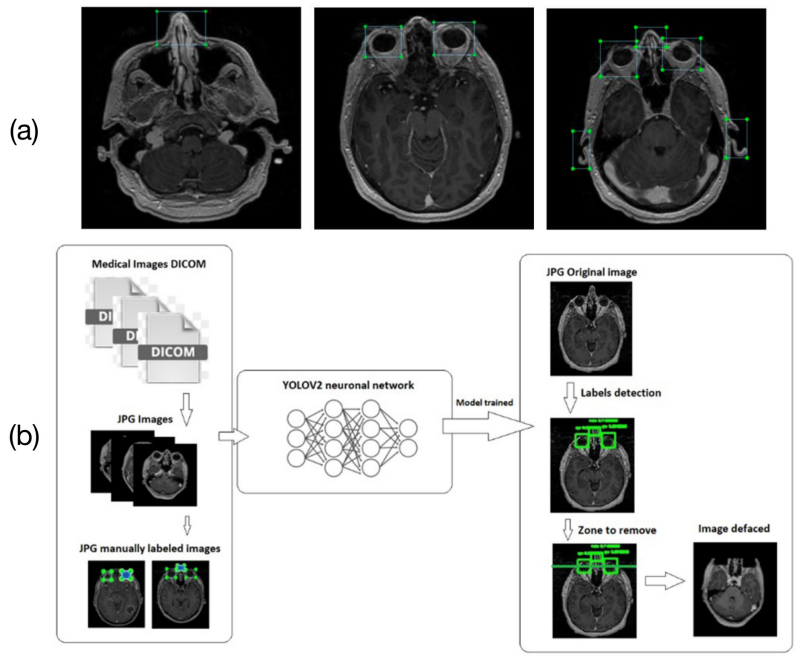


Fig. 1: The first step defacing workflow. After labelling, CNN was trained and then tested. (a)Images derived from DICOM data were manually labelled to identify facial regions. (b) A YOLOv2 detector was trained on local regions for the face removal workflow. The trained network located regions for removal to produce defaced images.

Image–mask correspondence was inspected visually in orthogonal views using FSL version 6.0.7.18, ITK-SNAP version 4.2.2 and 3D Slicer version 5.8.0. These checks complement comparisons of the geometry stored in the headers.

Segmentation procedure

Lesions were segmented on 3D-T1w+C images using either the in-house semiautomatic workflow described previously[33] or ITK-SNAP version 4.2.2, following the same procedure. An intensity threshold provided an initial delineation of the contrast-enhancing tumour volume. A biomedical engineer/applied mathematician (Y.Y.C.-S., J.P.-B., D.M.-G., I.F., B.O.-T., S.B.-V., M.P.-P., or V.M.P.-G.) then refined the contours on individual slices using tools for adding and removing pixels. This manual refinement aimed to improve the delineation of lesion boundaries and the representation of lesion morphology. The annotations distinguished contrast-enhancing tissue from the non-enhancing or necrotic components, with separate labels for each region. Each lesion retained the same identifier across follow-up examinations. Lesions with less than $\leq 2.5mm^3$ were excluded. The procedure is illustrated in Figure 3.

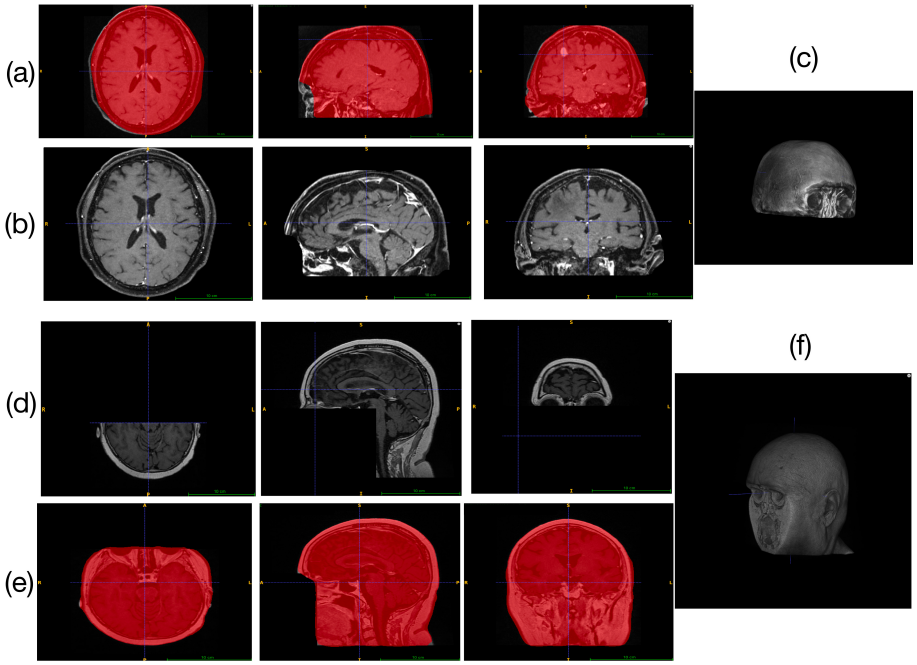


Fig. 2: Complementary defacing of 3D-T1w+C images. (a) Brain-mask boundary displayed in three orthogonal planes. (b) Image after mask-based processing. (c) 3-D volume defaced image. (d,e,f) Examples illustrating the orientation-dependent removal of facial regions in the initial workflow, motivating the complementary processing step.

Four researchers with more than seven years of experience in MRI analysis (Y.Y.C.-S., D.M.-G., J.P.-B., and V.M.P.-G.) cross-checked the annotations. The resulting masks underwent visual inspection and manual refinement in ITK-SNAP version 4.2.2. Difficult cases were reviewed by a neuroradiologist with 25 years of experience.

Morphological and radiomic feature extraction

Features were extracted from the 3D-T1w+C images and their lesion masks using PyRadiomics version 3.1.1. For each lesion observation, the contrast-enhancing and non-enhancing or necrotic labels were combined to define a single region of interest. Intensity normalisation used a brain mask and the z-score method implemented in the `intensity-normalization` Python package, version 2.2.4.

The extraction procedure yielded 107 features. The supplied configuration description lists 14 shape features, 18 first-order intensity statistics, 24 grey-level co-occurrence matrix features, 16 grey-level size zone matrix features, 16 grey-level run length matrix features, 14 grey-level dependence matrix features and 5 neighbouring grey tone difference matrix features. No image filters or voxel resampling were

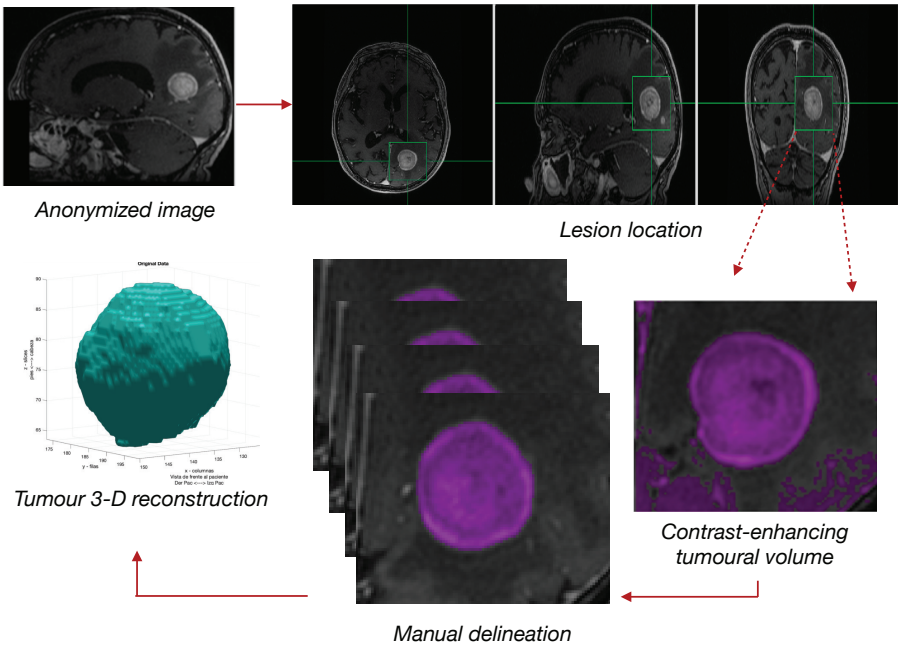


Fig. 3: Semiautomatic lesion segmentator. A lesion is located in orthogonal views of the 3D-T1w+C image. Intensity-based delineation is followed by manual correction on individual slices, and the resulting contours are combined into a three-dimensional tumour representation.

applied, and interpolation was disabled. The discretization bin width was 0.06 and the geometry tolerance was 0.01.

Imaging records

The imaging collection contains 3D-T1w+C, T2-W and FLAIR volumes. Sequence availability varies between examinations. Segmentation masks correspond to the 3D-T1w+C images used for annotation. Sequences, examination and lesion observations are distinct units: one examination may contain several sequences and multiple annotated lesions.

Clinical data

The clinical workbook contains a main worksheet, `MetMath`, and a coding worksheet, `Codes`. Clinical records are organised by lesion: the combination of the patient identifier (`OBTAI`) and lesion identifier (`id`) identifies each record. Patient-level information can therefore occur on several lesion rows and should not be counted as independent patient observations. Repeated treatment courses and MRI examination dates are stored in separate columns within each record. The value `n/a` denotes information that is not available.

Patient and lesion characteristics. The fields `Age-RM1` and `Sex` record the patient's age at the first MRI examination and sex (1, female; 2, male), respectively. The lesion fields comprise `id`, `Location`, and `Diagnosis date`. Location is recorded as text. Non-metastatic lesions are recorded when they are observed, indicating an Aneurysm, Meningioma, or Developmental Venous Anomaly. The primary tumour is described by `Type` and `Subtype`; the subtype codes must be interpreted together with the primary tumour type.

Primary tumour coding. The coding worksheet defines the following values for `Type`: 1, breast; 2, non-small-cell lung; 3, small-cell lung; 4, melanoma; 5, kidney; 6, colorectal; 7, bladder/urothelial; 8, unknown primary; 9, ovary; 10, oropharynx; 11, bone/soft-tissue sarcoma; 12, uterus; 13, esophagus; 14, neuroendocrine; 15, prostate; 16, pancreas; 17, cutaneous squamous cell carcinoma; and 18, gastric cancer. For breast cancer, the `Subtype` codes are 1, luminal A; 2, luminal B; 3, triple-negative; and 4, HER2. For lung cancer, the corresponding codes are 1, adenocarcinoma; 2, epidermoid carcinoma; 3, large-cell carcinoma; 4, large-cell endocrine carcinoma; 5, neuroendocrine carcinoma; 6, bronchioloalveolar carcinoma; and 7, squamous cell carcinoma. These categories retain the distinctions recorded in the supplied code sheet.

Molecular and immunohistochemical fields. The primary tumour block also contains fields labelled `EGFR`, `ALK`, `ROS1`, `KRAS`, `TTF1`, `Synaptophysin`, `Chromogranin`, `Calretinin`, `Vimentin`, `Mammaglobin`, `E-Cadherin`, `GATA3`, `PDL1 (>20%)`, `BRCA1`, `PAX8`, `RE`, `RP`, `HER2`, `BRAF`, `NRAS`, `CKIT`, `C-erbB2`, `p53`, `GDFP15`, `WT1`, `p63`, `CD10`, `CD56`, `CDX2`, `CK5/6`, `CK7`, `CK20`, `CK34`, `AE1/AE3`, `CK19`, and `p16`. Field names are reproduced as stored in the workbook to facilitate identification.

Treatment history and radiation necrosis. Two column groups record whole-brain radiotherapy (labelled `Whole-brain radiotherapy`) and two record radiosurgery. Each group contains `Dose/frac`, `Nfrac`, `Start date`, and `End date`, describing dose per fraction in Gy, number of fractions, and treatment dates. Separate date fields record radiation necrosis and surgery. Four additional groups, labelled `Systemic chemotherapy (1)` through `Systemic chemotherapy (4)`, contain `Drug`, `Start date`, and `End date` for the recorded systemic treatments. Drug or regimen information is stored as text.

Death and imaging follow-up. The `Exitus` group contains the date and coded cause of death. Cause codes are 1, intracranial progression; 2, systemic disease; 3, both systemic and intracranial disease; 4, other causes; and 5, unknown. The MRI follow-up block contains 14 date fields, `MR1`–`MR14`, providing slots for successive imaging examinations. The number of populated dates depends on the imaging available for each record.

Segmentation records

Segmentation masks contain separate integer labels for individual lesions and their tissue regions. Labels encode the lesion identifier followed by a region digit: 1 denotes contrast-enhancing tissue and 2 denotes non-enhancing or necrotic tissue. Lesion identity is retained across follow-up examinations. For intensity normalization and feature extraction, the two regions belonging to a lesion were merged into one region of interest; labels from different lesions were kept separate. A CSV table encoding the lesion

identifier and region digit is provided, ensuring the correct background label and representation of absent regions in the final mask files.

Acquisition metadata and feature records

The acquisition metadata table describes MRI sequence parameters, including field strength, echo and repetition times, slice thickness and inter-slice spacing. The feature table records the morphological and radiomic measurements extracted from each analysed lesion observation. These measurements refer to the combined lesion region described above and should be interpreted with the corresponding imaging and processing settings.

Data Records

The dataset is available on Zenodo [34]. It comprises data from all 443 patients in the cohort, including medical image data (MRI scans at baseline and at follow-up time-points, where available), clinical information, radiomic features, spatial information, and acquisition metadata. Clinical information was obtained from the collaborating institutions and organised by patient and lesion, available in the Excel workbook *('OBTAI_Clinical_Info.xls')*. The variables and coding are described in *Clinical data* section. De-identification began at the contributing institutions and was followed by removal of identifying image metadata and assignment of study-specific patient identifiers using the OBTAI prefix. Lesion identifiers were maintained across follow-up examinations. No changes were made to the clinical and imaging dates in the released files, thus within-patient time intervals were preserved. The dataset includes multi-parametric MRI scans. The variation in the acquisition metadata between sequences of the same type, as well as between different type of sequence, can be verified in the CSV table *('OBTAI_Metadata_Info.csv')*, which has separated tabs for each type of sequence. For each patient, MRIs and segmentations are available in NIfTI format after preprocessing, as described in the *Image conversion and spatial consistency* section. The coordinates of the raw DICOM files have been preserved, along with the geometry and spatial consistency, and can be verified using the spatial information *('OBTAI_Shape_Records.csv')*. This file also contains label consistency information for each study-specific patient identifier and date, as described in the *Segmentation records* section. Furthermore, the radiomic features have been registered in the *('OBTAI_Radiomic_Features.csv')* for every lesion identifier assigned for each OBTAI and preserved across its different time points, as described in *Clinical data collection and de-identification* section and *Morphological and radiomic feature extraction* section. The dataset has been categorised into two groups based on the available time points. The first group *('single_date')*, containing 227 patients, has only the diagnosis date available. This directory contains 23 batches from *('pack_singledate_batch_01.zip')* to *('pack_singledate_batch_23.zip')* clutching 22 groups of 10 OBTAIs and 1 pack of 7 cases. The second group *('multiple_dates')*, containing 216 patients, has both the diagnosis date and different follow-up time points available. This directory holds 22 clusters from *('pack_multidates_batch_01.zip')* to *('pack_multidates_batch_22.zip')* keeping 21 groups of 10 OBTAIs and 1 pack of 6

cases. Each of the 443 cases in the cohort is contained in a directory named with the OBTAI identifier and holding the MRIs scans available and the segmentation files per date. All cases in the dataset have at least the 3D-T1-w+C sequence available and its respective 3D segmentation file available. A nomenclature was set to distinguish between the OBTAI and observation dates, using the ISO 8601 basic format *'yyyymmdd'*, as well as the medical image data *'img'* and segmentation files *'msk'*. The 3D-T1-w+C sequence is named *'t1gdx'*, T2-W is called *'t2xxx'*, and FLAIR is labelled *'flair'*. For example, the *OBTAI2001* corresponding to the January 19 2015 observation with the 3D-T1-w+C sequence is shown in the *OBTAI2001* folder as *'OBTAI2001_20150119_t1gdx_img.nii'* and the corresponding segmentation mask is *'OBTAI2001_20150119_t1gdx_msk.nii'*, for patient *OBTAI2344* corresponding to the April 9 2019 observation with the 3D-T1-w+C sequence is shown in the *OBTAI2344* folder as *'OBTAI2344_20190409_t1gdx_img.nii'* and the corresponding segmentation mask is *'OBTAI2344_20190409_t1gdx_msk.nii'*, and so on. All files preserve the consistent OBTAI identifier and lesion identifier, as well as the follow-up date convention registered in the radiomic features records. This information is registered in the *'OBTAI'* variable, and the *'MRI1-MR14'* variable MRI follow-up block in the clinical information. Patient identifiers, lesion identifiers, and imaging time points provide the necessary levels of linkage to relate these components. Non-metastatic lesions are included in clinical data if they are observed, as described in *Patient and lesion characteristics* section. No source DICOM images are included in the dataset.

This study presents a dataset that supports automated image analysis and contributes to refined clinical diagnosis, prognostic stratification, and the development of non-invasive biomarkers. It achieves this by merging multicentre scanner variability, different primary tumour types, longitudinal continuity with unique lesion tracking, multiparametric MRI coverage and comprehensive radiomic and morphological profiling within a single framework.

Technical Validation

Clinical and imaging review

Patients had a pathologically established primary tumour and BMs confirmed by a radiation oncologist before inclusion. Eligibility and image quality were assessed by experienced members of the imaging team and cross-checked by another expert, following the data-curation workflow described previously [30]. Imaging review required the availability of a high-resolution 3D-T1w+C sequence and excluded studies with significant motion-related blurring or ghosting artefacts.

Segmentation review

All masks underwent the successive annotation, cross-checking, and clinical review steps described in the Segmentation procedure section. The segmentations were inspected in the axial, coronal, and sagittal planes and manually corrected where necessary using ITK-SNAP version 4.2.2 perfomed by four researchers (Y.Y.C.-S.,

D.M.-G., J.P.-B., and V.M.P.-G.) with more than 7 years of experience in MRI analysis . Difficult cases received additional review by a neuroradiologist (E.A.) with 25 years of experience.

Spatial consistency and software compatibility

The converted images and masks were visually checked in orthogonal planes to assess spatial correspondence. The NIfTI images and masks were also checked for readability in FSLeyes version 1.14.2, ITK-SNAP version 4.2.2 and 3D Slicer version 5.8.0. These checks establish compatibility with the software used for inspection; they do not quantify interobserver segmentation agreement. Quality-control outcomes, including image–mask geometry, identifier and date consistency, were assessed using SimpleITK version 2.0. A CSV table records geometry and label consistency together with the corresponding patient identifier and date.

Usage Notes

Linking patients, lesions and examinations

Users should link imaging, masks, clinical records and feature measurements using the released identifiers and examination information. Lesion identifiers are interpreted within a patient. Multiple lesions and repeated observations from the same patient are statistically dependent; clinical variables repeated across lesion rows must not be treated as additional patients. For machine-learning experiments, all observations from a patient should remain within the same training, validation or test partition to avoid information leakage.

Working with images and labels

Images and masks should be opened using software that respects NIfTI spatial metadata. Confirm alignment before extracting measurements or combining sequences. Reorientation to a common axis convention does not establish registration between different sequences or examinations. If additional resampling is required, use an interpolation method appropriate to the image type and preserve discrete mask labels, for example with nearest-neighbour interpolation. For lesion-level analyses, retain the distinction between enhancing and non-enhancing or necrotic labels unless the intended measurement requires their union.

Longitudinal analyses and radiomics

The available follow-up differs between patients, and treatment dates should be considered when interpreting changes in lesion size or morphology. Absence of a later observation does not establish lesion resolution. Similarly, an unavailable radiation necrosis entry should not automatically be interpreted as a confirmed negative outcome. The value `n/a` denotes unavailable information. Analyses requiring diagnostic outcome labels should specify their endpoint definitions and the supporting clinical evidence.

Radiomic measurements depend on acquisition, segmentation, intensity normalisation and discretisation. The supplied features should be used with the documented settings, and studies using other preprocessing choices should recompute the features consistently. Scanner and protocol differences should be considered when pooling observations or evaluating model transfer between centres.

Scope and limitations

The collection is retrospective, includes deceased patients, and was selected for available imaging of sufficient quality. It therefore should not be assumed to represent an unselected contemporary BM population. Follow-up and clinical-field completeness vary, and treatment allocation was not randomised. These properties should be considered when developing prognostic models, comparing treatments or interpreting associations. The dataset supports methodological research; claims of clinical predictive performance require an appropriate evaluation design and independent validation.

Data Availability

The dataset can be downloaded online directly from the repository: https://doi.org/10.5281/zenodo.23662223.

Code Availability

Processing used dicom2nifti 2.4.10, dcm2niix 1.0.20241211, FSL 6.0.7.18, PyDeface 2.0.2, NiBabel, ITK-SNAP 4.2.2, 3D Slicer 5.8.0, PyRadiomics 3.1.1 and `intensity-normalization` 2.2.4. The custom components include the initial defacing workflow, segmentation tools and processing scripts.

Acknowledgements

This work was partially supported by project PID2025-174928OB-I00, funded by Ministerio de Ciencia e Innovación/Agencia Estatal de Investigación, Spain (https://doi.org/10.13039/501100011033), and the European Regional Development Fund (ERDF, A way of making Europe). We acknowledge support from the Scientific Foundation of Asociación Española contra el Cáncer grant RENACER (coordinated projects AECC2023, grant ID PRYCO234528VALI).

Author Contributions

Y.Y.C.-S. and V.M.P.-G conducted the overall execution of the research. Y.Y.C.-S., B.O.-T., J.P.-B., D.M.-G., E.A. and V.M.P.-G. designed the research. Y.Y.C.-S., B.O.-T., J.P.-B., D.M.-G., M.P.-P., S.B.-V., I.F.-H., and V.M.P.-G. performed the segmentations. B.A., D.A., A.O.M., L.A.P.-R., E.G.P., M.L., N.C., F.N.-R., M.V.-D., B.L., Z.H.C.Z., A.R., R.M. and E.A. collected the data. J.D.V.-G. and D.M.-G. developed the code for the first anonymization step. Y.Y.C.-S. developed the code for the

second anonymization step. Y.Y.C.-S. developed the code for the conversion step and spatial consistency verification. Y.Y.C.-S. developed the code for morphological and radiomic feature extraction. Y.Y.C.-S., D.M.-G., J.P.-B. and V.M.P.-G. performed the final segmentation curation. E.A. reviewed conflicting and difficult segmentations. Y.Y.C.-S. and V.M.P.-G. wrote the paper. All authors revised and corrected the manuscript.

Competing Interests

No competing interests to declare.

Additional Information

Correspondence and request for material should be addressed to Y.Y.C.-S.. **Reprints and permissions information** is available at www.nature.com/reprints

Publisher's note Springer Nature remains neutral with regard to jurisdictional claims in published maps and institutional affiliations.

Open Access This article is licensed under a Creative Commons Attribution-NonCommercial-NoDerivatives 4.0 International License. This licence permits any noncommercial use, sharing, distribution and reproduction in any medium or format, as long as appropriate credit is given to the original author(s) and the source, a link is provided to the Creative Commons licence, and any modification of the licensed material is indicated. Under this licence sharing of adapted material derived from this Article or parts of it is not allowed. The images or other third party material in this article are included in the article's Creative Commons licence, unless indicated otherwise in a credit line to the material. If material is not included in the article's Creative Commons licence and your intended use is not permitted by statutory regulation or exceeds the permitted use, you will need to obtain permission directly from the copyright holder. Please read the full licence for further details at - http://creativecommons.org/licenses/by-ncnd/4.0/.

References

[1] Achrol, A.S., et al.: Brain metastases. Nature Reviews Disease Primers **5**(5) (2019) https://doi.org/10.1038/s41572-018-0055-y

[2] Valiente, M., *et al.*: The Evolving Landscape of Brain Metastasis. Trends in Cancer **4**(3), 176–196 (2018) https://doi.org/10.1016/j.trecan.2018.01.003

[3] Boire, A., Brastianos, P.K., Garzia, L., & Valiente, M.: Brain metastasis. Nature Reviews Cancer. **20**, 4–11 (2020) https://doi.org/10.1038/s41568-019-0220-y

[4] Vogelbaum, M.A., *et al.*: Treatment for Brain Metastases: ASCO-SNO-ASTRO Guideline. Journal of Clinical Oncology **40**(5), 492–516 (2022) https://doi.org/10.1200/jco.21.02314

[5] Brown, P.D., *et al.*: Effect of radiosurgery alone vs radiosurgery with whole brain radiation therapy on cognitive function in patients with 1 to 3 brain metastases: a randomized clinical trial. JAMA **316**, 401–409 (2016) https://doi.org/10.1001/jama.2016.9839

[6] K.R., F., J.R., .F.: Imaging of brain metastases. Surg Neurol Int **4**(4), 209–19 (2013) https://doi.org/10.4103/2152-7806.111298

[7] Pope, W.B.: Brain metastases: neuroimaging. Handb Clin Neurol **149**, 89–112 (2018) https://doi.org/10.1016/B978-0-12-811161-1.00007-4

[8] Zakaria, R., et al.: The role of magnetic resonance imaging in the management of brain metastases: diagnosis to prognosis. Cancer Imaging **14**(1) (2014) https://doi.org/10.1186/1470-7330-14-8

[9] Ocaña-Tienda, B., *et al.*: Growth dynamics of brain metastases differentiate radiation necrosis from recurrence. Neuro-Oncology Advances **149**, 179 (2023) https://doi.org/10.1093/noajnl/vdac179

[10] Kanakarajan, H., De Baene, W., Hanssens, P., & Sitskoorn, M.: Predicting local control of brain metastases after stereotactic radiotherapy with clinical, radiomics and deep learning features. Radiation Oncology **19**(1) (2024) https://doi.org/10.1186/s13014-024-02573-9

[11] Salbas, A., et al.: Temporal evolution of MRI findings and survival outcomes in patients with brain metastases after stereotactic radiosurgery. BMC Med Imaging **25**(1) (2025) https://doi.org/10.1186/s12880-025-01713-1

[12] Nowakowski, A., *et al.*: Radiomics as an emerging tool in the management of brain metastases. Neurooncology Adv **4**(1), 141 (2022) https://doi.org/10.1093/noajnl/vdac141

[13] Heugenhauser, J., et al.: Radiomics for risk stratification in brain metastases: potential in melanoma brain metastases. Clinical amp; Experimental Metastasis **43**(4) (2026) https://doi.org/10.1007/s10585-026-10422-0

[14] Salim, H.A., et al.: Mri radiomics for survival prediction in brain metastases: A machine learning analysis. AJNR. American journal of neuroradiology **ajnr.A9630**(Advance online publication) (2026) https://doi.org/10.3174/ajnr.A9630

[15] Grøvik, E., *et al.*: Deep learning enables automatic detection and segmentation of brain metastases on multisequence mri. Journal of magnetic resonance imaging

51(1), 175–182 (2020) https://doi.org/10.1002/jmri.26766

[16] Wang, T.W., et al.: Brain metastasis tumor segmentation and detection using deep learning algorithms: A systematic review and meta-analysis. Radiotherapy and oncology : journal of the European Society for Therapeutic Radiology and Oncology **190**(110007) (2024) https://doi.org/10.1016/j.radonc.2023.110007

[17] Link, K.E., *et al.*: Longitudinal deep neural networks for assessing metastatic brain cancer on a large open benchmark. Nat Commun **15**, 8170 (2024) https://doi.org/10.1038/s41467-024-52414-2

[18] Ocaña-Tienda, B., & Pérez-García, V.M.: Mathematical modeling of brain metastases growth and response to therapies: a review. Mathematical Biosciences **373**, 109207 (2024) https://doi.org/10.1016/j.mbs.2024.109207

[19] Stanford, AIMI.: BrainMetShare. https://aimi.stanford.edu/datasets/brainmetshare (accessed 24 September 2026) (2024)

[20] Rudie, J.D., et al.: The University of California San Francisco Brain Metastases Stereotactic Radiosurgery (UCSF-BMSR) MRI Dataset. Radiology: Artificial Intelligence **6**(2) (2024) https://doi.org/10.1148/ryai.230126

[21] Ramakrishnan, D., et al.: A large open access dataset of brain metastasis 3D segmentations on MRI with clinical and imaging information. Sci Data **11**(1) (2024) https://doi.org/10.1038/s41597-024-03021-9

[22] Moawad, A.W., *et al.*: The Brain Tumor Segmentation (BraTS-METS) Challenge 2023: Brain Metastasis Segmentation on Pre-treatment MRI. Machine Learning for Biomedical Imaging **2025**(December 2025), 204–247 (2025) https://doi.org/10.59275/j.melba.2025-9bd3

[23] Maleki, N., et al.: Analysis of the MICCAI Brain Tumor Segmentation–Metastases (BraTS-METS) 2025 Lighthouse Challenge: Brain Metastasis Segmentation on Pre- and Post-treatment MRI. Preprint at https://doi.org/10.48550/arXiv.2504.12527 (2025)

[24] Clark, K., *et al.*: The Cancer Imaging Archive (TCIA): Maintaining and Operating a Public Information Repository. J Dig Imaging **26**(6), 1045–1057 (2013) https://doi.org/10.1007/s10278-013-9622-7

[25] Chadha, S., et al.: MR Imaging and Segmentations with Matched Brain Biopsy Pathology Slides from Patients with Brain Metastases from Primary Lung Cancer (Brain-Mets-Lung-MRI-Path-Segs) (Version 2) [dataset]. The Cancer Imaging Archive. https://doi.org/10.7937/k0sm-y874 (2025)

[26] Wang, Y., et al.: Brain Tumor Recurrence Prediction after Gamma Knife Radiotherapy from MRI and Related DICOM-RT: An Open Annotated Dataset and

Baseline Algorithm (Brain-TR-GammaKnife) [Dataset]. The Cancer Imaging Archive. https://doi.org/10.7937/xb6d-py67 (2023)

[27] Taha, B.R., *et al.*: An integrated dataset of metastatic breast cancer to the brain with imaging, radiomics, and tumor genetics. Sci Data **12**, 1851 (2025) https://doi.org/10.1038/s41597-025-06066-6

[28] Gong, Z., et al.: A Multi-Center, Multi-Parametric MRI Dataset of Primary and Secondary Brain Tumors. Sci Data **11**(1) (2024) https://doi.org/10.1038/s41597-024-03634-0

[29] Nohel, M., *et al.*: BEAMSTER: Brain mEtAstases segMentation for STEreotactic Radiotherapy, A Retrospective MRI Dataset with Expert Segmentations. Sci Data (2026) https://doi.org/10.1038/s41597-026-07777-0

[30] Ocaña-Tienda, B., *et al.*: A comprehensive dataset of annotated brain metastasis mr images with clinical and radiomic data. Sci Data **10**, 208 (2023) https://doi.org/10.1038/s41597-023-02123-0

[31] Flouri, D., *et al.*: A longitudinal mri dataset of brain metastases with tumor segmentations, clinical & radiomic data. Sci Data **12**, 1828 (2025) https://doi.org/10.1038/s41597-025-06131-0

[32] Cox, S.N. B.: Official definition of the NIfTI-1 header. https://www.nitrc.org/docman/view.php/26/64/nifti1.h

[33] Pérez-Beteta, J., *et al.*: Tumor surface regularity at mr imaging predicts survival and response to surgery in patients with glioblastoma. Radiology **288**(1), 218–225 (2018) https://doi.org/10.1148/radiol.2018171051

[34] Calderón-Silva, Y.Y., et al.: OBTAI: A multicentre longitudinal brain metastasis imaging dataset with lesion segmentations and clinical data. Zenodo https://doi.org/10.5281/zenodo.23662223 (2026)